



Cite this: RSC Adv., 2017, 7, 53752

## Red phosphor based on $\text{Eu}^{3+}$ -isoelectronically doped $\text{Ba}_2\text{SiO}_4$ obtained via sol-gel route for solid state lightning†

 Airton G. Bispo Jr.<sup>ab</sup> Diego A. Ceccato,<sup>ab</sup> Sergio A. M. Lima <sup>ab</sup> and Ana. M. Pires <sup>ab</sup>

The present paper reports on the effect of  $\text{Eu}^{3+}$  concentration (1–5%, considering a charge compensation mechanism) on the structural, morphological and spectroscopic properties of  $\text{Ba}_2\text{SiO}_4$  produced by using a novel approach that involves an adapted sol-gel route. XRD data showed that high crystalline and single phase doped  $\text{Ba}_2\text{SiO}_4$  samples were prepared at lower calcination temperature (1100 °C) compared to the standard solid-state method (~1300 °C). FTIR, Raman and DRS analyses indicated that the  $\text{Ba}^{2+}$  replacement by  $\text{Eu}^{3+}$  ions causes punctual structural defects in the  $\text{Ba}_2\text{SiO}_4$  lattice, which particles observed by SEM imaging have irregular shape characteristics for the use of the acid-catalyzed sol-gel method. Optical bandgap values evaluated by DRS measurements of the red phosphors are smaller (~4.5 eV) than that of the nominally pure matrix (~5.8 eV), evidencing that  $\text{Eu}^{3+}$  ions increase  $\text{Ba}_2\text{SiO}_4$  structural/electronic defects. The detailed analysis of the  $f-f$   $\text{Eu}^{3+}$  narrow transitions in the photoluminescence spectra showed that doping ions occupy at least two non-equivalent sites without an inversion center in the  $\text{Ba}_2\text{SiO}_4$  host. Moreover, the 5% doped sample also exhibited a third  $\text{Eu}^{3+}$  anomalous site assigned to the  $\text{Eu}^{3+}-\text{O}^{2-}$  associates, which has a spectral behavior distinct from  $\text{Eu}^{3+}$  occupying ordinary host lattice sites. Finally, the 4%-doped sample exhibited the highest relative emission intensity while the 5%-doped, the highest quantum efficiency (72.6%) which qualifies these materials as potential candidates to be used as red phosphors for solid state lightning.

Received 21st September 2017

Accepted 14th November 2017

DOI: 10.1039/c7ra10494d

[rsc.li/rsc-advances](http://rsc.li/rsc-advances)

## Introduction

Nowadays the use of solid state devices for lighting is increasing drastically because of their advantages over incandescent and fluorescent light bulbs, *i.e.*, high brightness, mercury-free composition, relatively small size, low power consumption and long lifespan.<sup>1–3</sup> In this context, LED lights stand out due to their relative ease of device manufacture and versatility of application mainly in digital displays, liquid crystal devices, headlight vehicles, road lights, public and residential lighting.<sup>4–6</sup> LED operation is based on spontaneous light emission in semiconductors originating from electron–hole recombination produced by the passage of electric current.<sup>7</sup> Thus, luminescent nanostructured phosphors have taken an important role in the advance of solid devices technology because they exhibit great potential for application in high-performance

displays like white LEDs (WLEDs).<sup>8,9</sup> The commercially available WLEDs are based on two different design approaches (i) based on the white emission of the semiconductor or, (ii) based on a combination of colors emitted by different phosphors excited by the semiconductor. For the second approach, the combination of green, red and/or yellow phosphors plus a blue/near UV emission of the semiconductor gives the observer a sense of white light when they simultaneously emit.<sup>10</sup>  $\text{Y}_3\text{Al}_5\text{O}_{12}:\text{Ce}^{3+}$ (YAG:Ce<sup>3+</sup>) and  $(\text{Sr},\text{Ba})\text{SiO}_4:\text{Eu}^{2+}$  are reported in the literature as the main yellow phosphors,  $\text{Lu}_3\text{Al}_5\text{O}_{12}:\text{Ce}^{3+}$ (LuAG:Ce<sup>3+</sup>) and  $(\text{Ba},\text{Sr})\text{SiO}_4:\text{Eu}^{2+}$  as the green ones, and  $(\text{Sr},\text{Ba})_2\text{Si}_5\text{N}_8:\text{Eu}^{2+}$  and  $(\text{Sr},\text{Ca})\text{SiAlN}_3:\text{Eu}^{2+}$  as the main red emitters.<sup>11</sup> The most common WLED commercially available in the present days, is based on a combination of a blue LED and the yellow phosphor YAG:Ce<sup>3+</sup>.<sup>11</sup> However, such device has poor color-rendering index (CRI) and low stability of the correlated color temperature (CCT). In this sense, the use of ultraviolet LEDs are emerging because the human eye does not see the UV light, solving the color-rendering index problem.<sup>12</sup> Examples of UV LEDs include: GaN and AlN with bandgap equal to 3.4 eV (362 nm) and 6.2 eV (200 nm). The last one is suitable to excite Eu(III) phosphors as  $\text{Ba}_2\text{SiO}_4:\text{Eu}^{3+}$ .<sup>13</sup>

Materials based on silicates have been considered an especial class of compounds with great potential for application in

<sup>a</sup>São Paulo State University (Unesp), School of Technology and Sciences, R. Roberto Simonsen, 305, Presidente Prudente, SP 19060-900, Brazil. E-mail: [anapires@fct.unesp.br](mailto:anapires@fct.unesp.br); Tel: +55 1832295748

<sup>b</sup>São Paulo State University (Unesp), Institute of Biosciences, Humanities and Exact Sciences, São José do Rio Preto, SP, 15054-000, Brazil

† Electronic supplementary information (ESI) available. See DOI: [10.1039/c7ra10494d](https://doi.org/10.1039/c7ra10494d)



optical devices like white LEDs, especially those doped with lanthanide ions, due to their high thermal and chemical stability, transparency for visible light, relative low phonon frequency, and ease preparation.<sup>14–16</sup> For instance, Eu<sup>2+</sup>-doped Ba<sub>2</sub>SiO<sub>4</sub> phosphors have been considered for LED application, but little attention has been paid for Eu<sup>3+</sup>-doped Ba<sub>2</sub>SiO<sub>4</sub>,<sup>11</sup> since they cannot be efficiently excited by near UV or blue light. However, with the emergence of high energy UV LEDs chip in the last years, Eu<sup>3+</sup>-phosphors are being considered as LEDs components.<sup>13</sup> Eu<sup>3+</sup> ion is a red emitter and also may act as a structural probe in phosphors due to its well-known spectroscopic behavior exhibiting optical transitions that are usually narrow and sensitive to the crystal field around the ion.<sup>17–19</sup> Eu<sup>3+</sup>-doped orthosilicate phosphors, such as Ba<sub>2</sub>SiO<sub>4</sub> and BaZnSiO<sub>4</sub>, synthesized by conventional solid state reaction had already been investigated and showed interesting optical properties.<sup>20–22</sup> However, reports on the use of Eu<sup>3+</sup> in such systems is uncommon since Eu<sup>2+</sup> ions are more suitable to substitute for divalent barium in silicate lattices synthesized under reducing atmosphere yielding a phosphor with green-bluish emission. In addition, the majority of reports involves phosphors obtained *via* solid state synthesis instead of the sol-gel methodology, which is considered a versatile and convenient low-temperature process to produce different type of materials, including the luminescent ones.<sup>23–25</sup> For the best of our knowledge, there is no paper reported in the literature about the use of the sol-gel route to prepare Eu<sup>3+</sup>-doped orthosilicates, while several papers report on the obtainment of Eu<sup>2+</sup>-doped orthosilicates, such as the sub-microsized (Ba,Sr)<sub>2</sub>SiO<sub>4</sub>:Eu<sup>2+</sup> phosphors prepared by the sol-gel/Pechini method and their solid solutions,<sup>26,27</sup> and the Eu<sup>2+</sup>-doped M<sub>2</sub>SiO<sub>4</sub> (M = Ca, Ba) phosphors obtained by a rapid microwave-assisted approach.<sup>28</sup> Complementally, we have recently published a study showing a successful synthesis of barium- and europium-doped silica xerogel obtained *via* the sol-gel process, and its use as an electro catalytic sensor.<sup>29</sup> Furthermore, we have also found out that this xerogel can be a suitable precursor for obtaining either doped or undoped Ba<sub>2</sub>SiO<sub>4</sub> phase. However, one of the challenges to be overcome is the sol-gel route adjustment to yield single phased silicate red phosphor avoiding undesirable spurious phases, such as carbonate one. Therefore, considering the advantages of the sol-gel synthesis and the lack of information in the literature related to Eu<sup>3+</sup>-doped barium silicate, we report in this paper the synthesis of Ba<sub>2</sub>SiO<sub>4</sub>:Eu<sup>3+</sup> red phosphor *via* the sol-gel route, and its morphological, structural and spectroscopic characterization aiming the improvement of its properties for use in optical devices, such as white LEDs.

## Experimental

Pure Ba<sub>2</sub>SiO<sub>4</sub> and Eu<sup>3+</sup>-doped Ba<sub>2</sub>SiO<sub>4</sub> were synthesized *via* an adapted sol-gel route<sup>29</sup> by using Ba(CH<sub>3</sub>COO)<sub>2</sub> (VETEC, 99.9%), Eu<sub>2</sub>O<sub>3</sub> (Aldrich, 99.99%), C<sub>8</sub>H<sub>20</sub>O<sub>4</sub>Si, (TEOS, Fluka, 99.9%), and CH<sub>3</sub>COOH (VETEC, 97%), as starting reactants. Europium acetate was prepared by dissolving europium oxide in stoichiometric quantities of hot acetic acid. For the synthesis of the

gel, stoichiometric amount of barium and europium acetate were dissolved in 10 mL of acetic acid in order to obtain 2.0000 g of Ba<sub>x</sub>Eu<sub>y</sub>SiO<sub>4</sub>. The Eu<sup>3+</sup> concentration was isoelectronically varied from 1 to 5%, *i.e.*, keeping the same overall charge in the Ba<sub>2</sub>SiO<sub>4</sub> matrix in relation to the Ba<sup>2+</sup> ion, according to the Ba<sup>2+</sup>, Eu<sup>3+</sup> and SiO<sub>4</sub><sup>4-</sup> charges (3n<sub>Eu</sub><sup>3+</sup> + 2n<sub>Ba</sub><sup>2+</sup> = +4, where n<sub>Ba</sub><sup>2+</sup> and n<sub>Eu</sub><sup>3+</sup> are the mol number of Ba<sup>2+</sup> and Eu<sup>3+</sup>, respectively). The calculated amounts of reagents and the detailed description of this calculus can be found in the ESI, Table ES1.† Then, a stoichiometric amount of TEOS dissolved in 10 mL of isopropyl alcohol was added. Finally, 0.4 mL of deionized water was introduced to initiate hydrolysis reactions. Acetic acid was used as both solvent and catalyst. The mixture was kept under stirring for 4 h at room temperature until gel formation; the gel was thermally treated at 100 °C in a static air atmosphere for 2 hours to allow solvent evaporation resulting in the xerogel phases. Then, xerogel precursor samples were pre-calcinated at 450 °C in a circulating air atmosphere with a heating ramp of 10 °C min<sup>-1</sup> for 2 hours, and then, calcinated at 1100 °C in a circulating air atmosphere with a heating ramp of 10 °C min<sup>-1</sup> for 2 hours. The calcination temperature was previously determined by thermal analysis measurements.<sup>29</sup> A non-doped sample was synthesized as a control.

All samples were structurally characterized by X-ray diffraction (XRD) using a SIEMENS diffractometer model D5000, CuK $\alpha$  radiation ( $\lambda = 1.5405 \text{ \AA}$ ), a  $2\theta$  range of 20–50°, an increment of 0.02° and integration time of 1 s. The crystallite size of all produced powder samples was evaluated *via* Scherrer's method described in the ESI.†

Samples were also molecularly and morphologically investigated by Fourier Transform Infrared Spectroscopy (FTIR) using a Shimadzu Spectrometer IRAffinity-1 model and the samples were prepared in KBr pellets. Raman spectroscopy using a micro-Raman spectrograph Renishaw, in-Via model, with a 514 nm laser and scanning electron microscopy (SEM) using a Carls Zeiss model EVO LS15 microscope with a detector of secondary electrons (SE) in high vacuum and constant temperature.

The optical behavior of all samples was checked by diffuse reflectance spectroscopy in the UV-Vis region (DR) using a spectrometer Cary 500 Scan model (UV-VIS-NIR spectrophotometer) and also by photoluminescence measurements at room temperature carried out in a Horiba Jobin Yvon spectrometer Fluorolog-3 with a Xe lamp (450 W) source with double excitation monochromator. Emission lifetime was evaluated using a phosphorimeter equipped with Xe (5 J per pulse) lamp.

## Results

The X-ray patterns of undoped and Eu<sup>3+</sup>-doped (1–5%) samples calcined at 1100 °C, Fig. 1(a), correspond to the single-phase orthorhombic Ba<sub>2</sub>SiO<sub>4</sub> ( $P_{\text{nam}}$ ) (JCPDS 26-1403, number 62) crystalline phase. With regard of the limit detection of this technique, no diffraction peaks characteristic of the europium, barium, or silicon oxides were detected, which corroborate for the fact that Eu<sup>3+</sup> ion is inserted into the Ba<sub>2</sub>SiO<sub>4</sub> lattice. Interplanar distance, full width at half maximum and crystallite



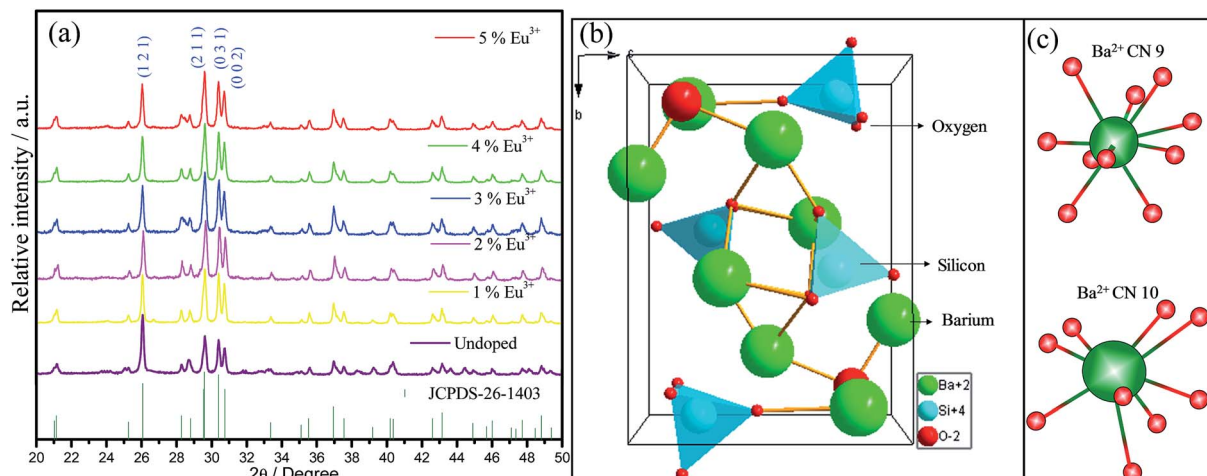


Fig. 1 (a) Powder X-ray diffractograms of all samples obtained via the sol-gel route from xerogel precursors calcinated at 1100 °C for 2 hours. (b) Ba<sub>2</sub>SiO<sub>4</sub> unit cell representation, based on the CIF file available on Inorganic Crystal Structure Database (ICSD); (c) representation of the two Ba<sup>2+</sup> ion sites, with coordination number of 9 and 10.

size data for all samples are shown in Table 1. Since no significant shifts for interplanar distances are observed, it is possible to suggest that Eu<sup>3+</sup> ions probably are occupying Ba<sup>2+</sup> sites in Ba<sub>2</sub>SiO<sub>4</sub> network. The low FWHM values confirm the formation of highly crystalline material for all samples, showing that the sol-gel method was efficient to the synthesis of well-crystallized Ba<sub>2</sub>SiO<sub>4</sub>:Eu<sup>3+</sup> under lower calcination temperature when compared to other routes such as solid-state reactions reported by A. M. Pires *et al.* (1200 °C for 12 hours),<sup>21</sup> Z. Wang *et al.* (1300 °C for 3 hours),<sup>22</sup> and M. Zhang *et al.* (1573 K for 6 hours).<sup>30</sup> The crystallite size values shown in Table 1 are comparable to the one of other oxide compounds prepared by

sol-gel method with high annealing temperatures (>1000 °C).<sup>31,32</sup> For some samples it is observed a preferential growth of certain crystallographic planes, indicating that the crystallites are not spherical. The crystallite size does not vary for the (1 2 1) plan, it increases when the Eu<sup>3+</sup> concentration increases for the (2 1 1) plan and it increases for the samples with 1, 4 and 5% for the plan (0 3 1). These modifications can be correlated to the defects generated in the Ba<sub>2</sub>SiO<sub>4</sub> lattice.

The Ba<sub>2</sub>SiO<sub>4</sub> lattice structure and the Ba<sup>2+</sup> and Si<sup>4+</sup> sites are illustrated in Fig. 1(b). This schematic representation is in accordance with K. A. Denault *et al.*<sup>33</sup> that described the Ba<sub>2</sub>SiO<sub>4</sub> structure as having two coordination sites for Ba<sup>2+</sup> ion, the largest one with coordination number (CN) 10, and the smallest structurally distorted with CN 9. The CN 10 site forms a chain along *c*-axis while the 9-coordinated sites form chains of Ba<sup>2+</sup> ions along the *b*-axis.<sup>34</sup> Thus, Eu<sup>3+</sup> ions must occupy both sites with CN 9 and 10. Due to the charge compensation mechanism considered in the present work, it is feasible to say that the Eu<sup>3+</sup> ions non-equivalently replace Ba<sup>2+</sup> ions. Two Eu<sup>3+</sup> ions are needed to substitute three Ba<sup>2+</sup> ions and, as consequence, one vacancy defect of  $V'_{\text{Ba}}$  with two negative charges is formed, and two positive defects of  $\text{Eu}_{\text{Ba}}^+$  are created, as it is shown in eqn (1).<sup>35</sup>

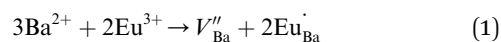


Table 1 Interplanar distance, full width at half maximum and crystallite size for the three most intense plans of the samples

Plan	Crystallite size/nm		Crystallite size/nm			
	<i>d</i> /Å	FWHM/°	<i>d</i> /Å	FWHM/°		
<b>5% Eu<sup>3+</sup></b>						
(1 2 1)	3.41	0.166	49	3.41	0.165	49
(2 1 1)	3.01	0.215	41	3.01	0.208	40
(0 3 1)	2.93	0.183	55	2.94	0.180	45
<b>4% Eu<sup>3+</sup></b>						
(1 2 1)	3.42	0.167	49	3.41	0.166	49
(2 1 1)	3.01	0.215	39	3.01	0.224	37
(0 3 1)	2.93	0.193	42	2.93	0.197	41
<b>3% Eu<sup>3+</sup></b>						
(1 2 1)	3.42	0.167	49	3.41	0.166	49
(2 1 1)	3.01	0.215	39	3.01	0.224	37
(0 3 1)	2.93	0.193	42	2.93	0.197	41
<b>2% Eu<sup>3+</sup></b>						
(1 2 1)	3.41	0.166	49	3.41	0.168	49
(2 1 1)	3.01	0.209	39	3.01	0.223	37
(0 3 1)	2.94	0.180	46	2.93	0.188	44
<b>1% Eu<sup>3+</sup></b>						
(1 2 1)	3.41	0.166	49	3.41	0.168	49
(2 1 1)	3.01	0.209	39	3.01	0.223	37
(0 3 1)	2.94	0.180	46	2.93	0.188	44
<b>Ba<sub>2</sub>SiO<sub>4</sub> (JCPDS 26-1403)</b>						
(1 2 1)	3.41	—	—			
(2 1 1)	3.01	—	—			
(0 3 1)	2.94	—	—			

The  $V'_{\text{Ba}}$  vacancies cause a local expansion in the Ba<sub>2</sub>SiO<sub>4</sub> lattice due to the repulsion of the oxi negative charges, and the Eu<sub>Ba</sub> defects cause a local compression in the lattice due to the increase of the positive charge in that site. This compression also occurs because Eu<sup>3+</sup> ions are smaller than Ba<sup>2+</sup>, as shown in Table 2. However, even that Eu<sup>3+</sup> is smaller than Ba<sup>2+</sup>, the substitution is favored since the difference ( $D_r$ ) between both ions radii is smaller than 30%.<sup>21</sup> Due to the large difference between the ionic radii of Eu<sup>3+</sup> and Si<sup>4+</sup> (~215%), the substitution of Si<sup>4+</sup> by Eu<sup>3+</sup> is unlikely.



**Table 2** Ionic radii, bond distance and radii difference ( $D_r$ ) between  $\text{Eu}^{3+}$  and  $\text{Ba}^{2+}$  ions in  $\text{Ba}_2\text{SiO}_4$  host<sup>21</sup>

Cation	Radius/pm (CN)	$D_r/$ %	Bond (CN)	Bond distance/pm
Ba	166 (10)		Ba–O (10)	298.3
Ba	161 (09)		Ba–O (09)	282.4
Si	40 (04)		Si–O	163.2
Eu	126 (09)	21.1%		
Eu	131 (10)	21.1%		

Since both size and shape of phosphor materials are of great importance for their potential applications, the morphology of the phosphors has been elucidated using scanning electron microscopy. SEM images of phosphors viewed in Fig. 2 show that all samples, independently on the presence, or amount of doping ion, exhibit the formation of aggregate particles with irregular shape. The doping does not lead to appreciable modification in the particle shape or size, but for the doped samples, nanowires on the particle surface are noted, as it can be seen in the magnified SEM images showed in the ESI, Fig. ES1.† These nanowires increase the particle surface area, enhancing the surface defect concentration, since more superficial sites with incomplete coordination sphere can be formed, which cause great influence in the spectroscopic properties of the material, as will be presented latter on. Many authors have attributed the degree of agglomeration and irregular morphology to the sol–gel method catalyzed by acid.<sup>36–38</sup> The grain size viewed in SEM images is much higher than the crystallite size obtained from XRD indicating that the agglomerated particles observed in the SEM images are formed by an arrangement of several nanocrystallites. Also, energy-dispersive X-ray spectroscopy (EDS), Fig. ES2,† confirm the presence of the elements Ba, Eu and Si on the particles surface and the chemical mapping performed by EDS, Fig. ES3,† shows their homogeneous distribution in an agglomerate of particles.

FTIR spectra for the prepared  $\text{Eu}^{3+}$ -doped and undoped  $\text{Ba}_2\text{SiO}_4$  samples are shown in Fig. 3. They exhibit bands assigned to the vibrational mode related to the silicate tetrahedron. In orthosilicate structures,  $\text{SiO}_4^{4-}$  complex anions are not linked but surrounded by  $\text{Ba}^{2+}$  cations and the chemical bond distance between Si and O is shorter than the distance between metal and oxygen. Therefore, internal modes for  $[\text{SiO}_4]$  are almost independent of external vibrations. In orthosilicate structures  $[\text{SiO}_4]$  internal modes are split because of their site symmetry (crystal field splitting) and unit-cell space symmetry (Davydov's splitting), which depends on the mixed anion–cation vibrations whereas crystal field splitting depends on anion internal force field change.<sup>39</sup>  $[\text{SiO}_4]$  tetrahedron has four genuine vibrational modes represented in the eqn (2).<sup>39</sup>

$$\Gamma_{\text{vib}} = 1\text{A}_1 + 1\text{E} + +2\text{F}_2 \quad (2)$$

Two genuine vibration modes are allowed by the selection rule for IR spectroscopy: ( $\nu_3$ ) asymmetric stretching and ( $\nu_4$ ) deformation, both  $\text{F}_2$  modes ( $\sim 916$  and  $\sim 497 \text{ cm}^{-1}$ ). The ( $\nu_1$ ) symmetric stretching and ( $\nu_2$ ) deformation,  $\text{A}_1$  and  $\text{E}$  modes, respectively, are not allowed by the selection rules, yet  $\text{A}_1$  mode is detected in the spectra with relatively low intensity ( $\sim 822 \text{ cm}^{-1}$ ), due to symmetry distortion. In addition carbonate group vibrational modes are also observed in all IR spectra and they can be assigned to the presence of carbonate ions on the surface of the particles despite of the fact that no carbonate phase is observed in XRD data, considering the technique detection limit of 1 wt% and the carbonate degree of crystallinity. Taking into account that the particles exhibit an active surface during the cooling step after the calcination process, the particles can react with atmospheric  $\text{CO}_2$  to form carbonate. Besides that, this carbonate should not be an amorphous phase formed during the synthesis because the baselines in XRD are

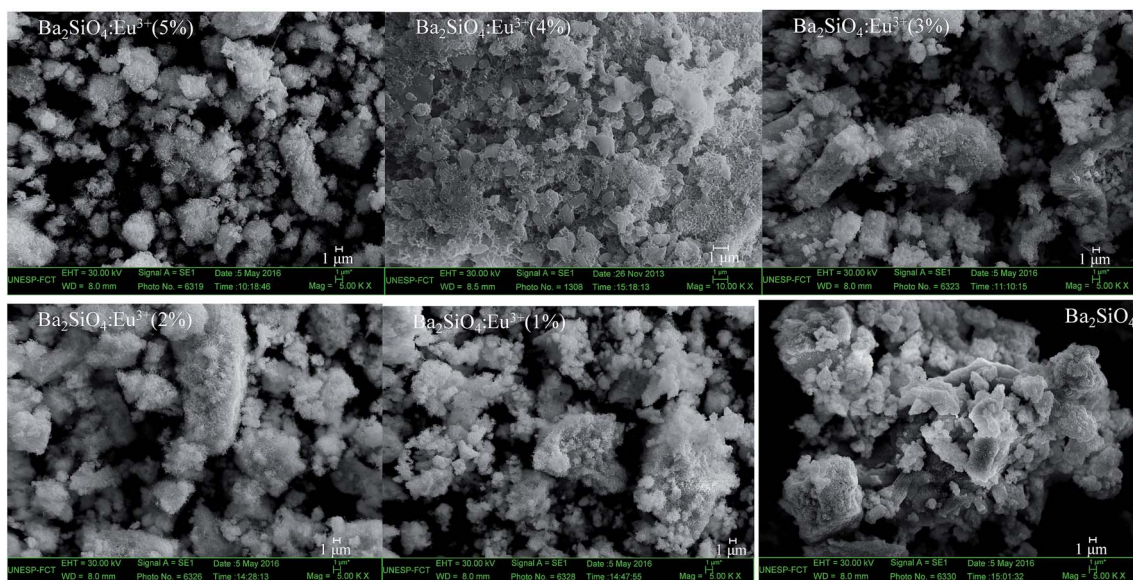


Fig. 2 Scanning electron microscopy images of undoped and  $\text{Eu}^{3+}$ -doped  $\text{Ba}_2\text{SiO}_4$  prepared by sol–gel method.

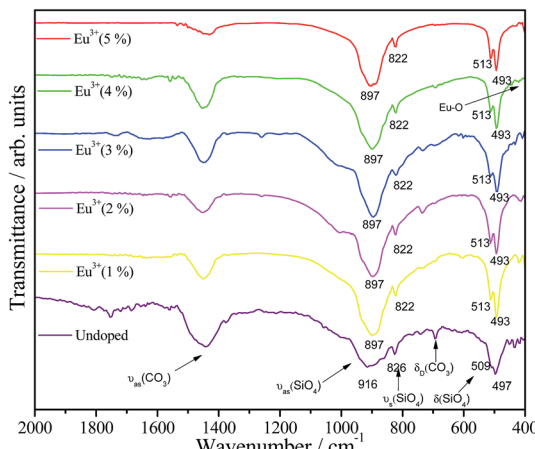


Fig. 3 FTIR spectra of undoped and  $\text{Eu}^{3+}$ -doped  $\text{Ba}_2\text{SiO}_4$  in KBr pellets.

well defined, indicating the absence of any cluster of amorphous material in the final product.

Still considering FTIR spectra in Fig. 3, it is observed that the undoped silicate exhibits a small shift for  $\nu_{\text{as}}$  ( $\sim 916 \text{ cm}^{-1}$ ),  $\nu_s$  ( $\sim 826 \text{ cm}^{-1}$ ) and  $\delta$  ( $\sim 509$  and  $\sim 497 \text{ cm}^{-1}$ ) [ $\text{SiO}_4$ ] bands compared to the doped samples. These small shifts suggest the existence of uniform stresses in the network, which are generally associated with defects in the material, confirming the proposition of defects that arise from the doping. These defects can cause a shortening of the Si–O bond around  $\text{Ba}^{2+}$  vacancies and an enlargement around  $\text{Eu}^{3+}$  sites, which is responsible for the observed vibrational modes displacements in relation to the undoped sample.<sup>40</sup> However, as the amount of europium is very lower than the amount of  $\text{Ba}^{2+}$  and  $\text{SiO}_4$ , these defects are local and do not cause extended deformation in the  $\text{Ba}_2\text{SiO}_4$  lattice, since the same number of vibrational modes was observed after the doping. Furthermore, the rigid second coordination sphere of the  $\text{Eu}^{3+}$  ion counteracts the expansions or compressions in the  $\text{Eu}^{3+}$  sites. The impacts of the defects around  $\text{Eu}^{3+}$  ions will be better discussed using the Judd–Ofelt intensity parameters in the PL results.

Raman spectra for undoped and doped- $\text{Ba}_2\text{SiO}_4$  samples are shown in Fig. 4. The bands observed at  $910$ ,  $886$ ,  $851$ ,  $821$ ,  $519$ ,  $597$ ,  $370$ , and  $350 \text{ cm}^{-1}$  are assigned to the vibrational modes related to the silicate tetrahedron.<sup>39</sup> Also, the absence of bands at  $559$ ,  $425$ ,  $385$ ,  $339$ , and  $289 \text{ cm}^{-1}$  characteristics of  $\text{Eu}_2\text{O}_3$  confirms the formation of a solid solution.<sup>41</sup> Full width at half maximum, band area, position and height for the ( $\nu_1$ )  $\nu_s$  ( $821 \text{ cm}^{-1}$ ) and ( $\nu_3$ )  $\nu_{\text{as}}$  ( $910$ ,  $886$ , and  $851 \text{ cm}^{-1}$ ) vibrational modes are listed in the ESI, Table ES2.† These bands do not exhibit shifts when the dopant is inserted in the matrix. However, the full width at half maximum, band area and height for the Eu-doped phosphors are different when compared to the undoped matrix. These modifications can be assigned to soft structural defects caused by the doping.

UV-Vis diffuse reflectance (DRS) spectra for undoped and  $\text{Eu}^{3+}$ -doped  $\text{Ba}_2\text{SiO}_4$  samples are viewed in Fig. 5(a), and also a magnification from  $310$  to  $500 \text{ nm}$  range is provided in

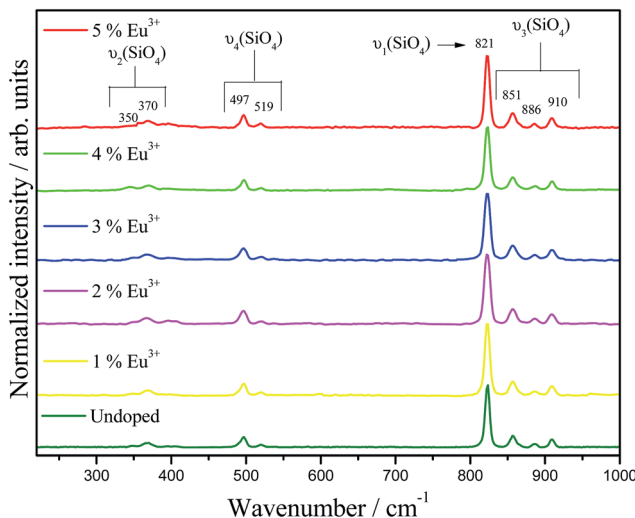


Fig. 4 Room temperature Raman spectra of  $\text{Ba}_2\text{SiO}_4:\text{Eu}^{3+}$  phosphors. Laser  $514 \text{ nm}$ .

Fig. 5(b). Doped samples show  $\text{Eu}^{3+}$  ion characteristic absorption lines at  $320$ ,  $362$ ,  $395$  and  $467 \text{ nm}$  assigned to the transitions from the ground state  $^7\text{F}_0$  to the  $^5\text{H}_J$ ,  $^5\text{D}_4$ ,  $^5\text{L}_6$  and  $^5\text{D}_2$  excited states, respectively. In addition, a smooth broad band observed at  $360 \text{ nm}$  is assigned to  $\text{Ba}_2\text{SiO}_4$  absorption,<sup>42</sup> and it can be related to the presence of traps or intrinsic defects in the matrix. These defects may be generated, among other causes, by the thermal decomposition of organic material or by products of the sol–gel synthesis during the  $\text{Ba}_2\text{SiO}_4$  lattice formation or through the calcination of samples.<sup>43</sup> In addition, for the doped samples, the region corresponding to the matrix band, that is better viewed in Fig. 5(b), has its reflectance decreased, which means a greater absorption in relation to the undoped sample, except for the 5%-doped sample. This behavior indicates that  $\text{Eu}^{3+}$  is contributing for the formation of defects in the  $\text{Ba}_2\text{SiO}_4$  lattice, corroborating with FTIR and Raman data. A careful analysis of Fig. 5(b) reveals that for the sample doped with  $4$ ,  $3$ ,  $2$  and  $1\%$ , the defect band intensity is constant and decreases for the sample doped with  $5\%$ . Therefore, it is possible to conclude that the sample with  $5\%$  of doping ions shows the lowest concentration of defects in the network. Therefore it is possible to conclude that the sample with  $4\%$  of doping ions shows the higher concentration of defects in the network. Another effect that can contribute to doped-phosphors defect formation increasing is the superficial defects, as evidenced by SEM images, Fig. 2.

The DR spectra also exhibit a strong and sharp absorption in the higher energy region with maximum near  $225 \text{ nm}$  related to transitions of the valence band (VB) and conduction band (CB) that corresponds to the bandgap of the material. Zhang *et al.* reported diffuse reflectance measurements for  $\text{Ba}_2\text{SiO}_4$  synthesized *via* solid state and the DR spectrum profile recorded by them matches with those showed here for samples obtained *via* the sol–gel route, except for slight differences that arise from the discrete morphology related to each synthetic methodology that directly affects sample reflection profile.<sup>42</sup>



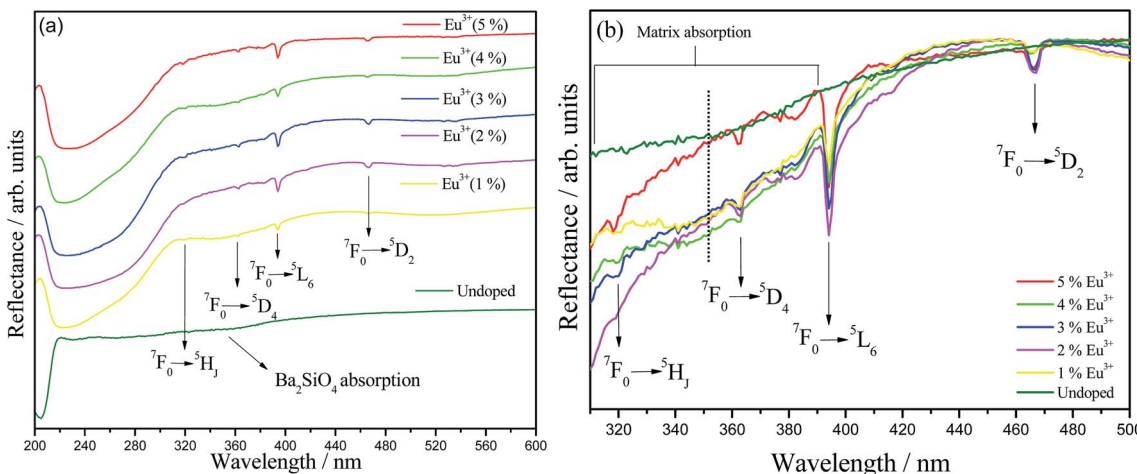


Fig. 5 (a) UV-Vis diffuse reflectance spectra of undoped and Eu<sup>3+</sup>-doped Ba<sub>2</sub>SiO<sub>4</sub> prepared by sol-gel method. (b) Magnification of the region between 310–500 nm.

Bandgap values of the Eu<sup>3+</sup> doped and undoped Ba<sub>2</sub>SiO<sub>4</sub> samples were also evaluated by using diffuse reflectance data through a graphic of  $(\alpha h\nu)^n$  versus the energy of the incident photon ( $h\nu$ ), where  $n$  equals 2 for direct transition and 0.5 for indirect transition.<sup>44</sup> The value of  $\alpha$  is the ratio of the absorption and scattering coefficients according to the Kubelka–Munk's approximation,<sup>45</sup> eqn (3).

$$\alpha = \frac{K}{S} = \frac{(1 - R)^2}{4R} \quad (3)$$

where  $R$  is the reflectance observed for the different incident energies. The obtained plots are viewed in the ESI, Fig. ES4,† whereas the curve extrapolation to the ordinate zero value provided the estimated bandgap energy. A complementary study showed that the samples exhibited a more suitable profile considering direct transitions (Fig. ES5†), from which the bandgap values listed in Table 3 were estimated. S. Z. Karazhanov *et al.*<sup>46</sup> reported bandgap values for Zn<sub>2</sub>SiO<sub>4</sub> between 5.5 and 6.2 eV, showing that this class of material has relatively high bandgap values. The analysis of these values indicates that the presence of dopant ions decreases the bandgap. This effect is expected since the replacement of Ba<sup>2+</sup> by Eu<sup>3+</sup> in the crystalline structure of the material will generate new energy levels, particularly the O<sup>2-</sup> → Eu<sup>3+</sup> charge transfer band, in between the valence and the conduction band of pure Ba<sub>2</sub>SiO<sub>4</sub> that will be responsible for the decrease in the bandgap values of the

doped materials. Also, the bandgap decrease is assigned to the surface defect concentration enhance for the doped samples, increasing the defect level concentration lying between the VB and CB. The modifications in the doped samples can be correlated to small changes on the particle surface which, in this case, is difficult to quantify due to the high agglomeration degree of the particles.

The excitation and emission spectra at room temperature of all europium(III) doped barium silicate samples are viewed in Fig. 6(a) and (b), respectively. A broad Eu<sup>3+</sup>–O<sup>2-</sup> charge transfer band (CT) is observed below 300 nm in all excitation spectra as well as the expected narrow lines with lower relative intensity related to the  $f$ - $f$  Eu<sup>3+</sup> transitions that are forbidden by Laporte's parity selection rule. Also, the phosphors can efficiently be excited by UV light source, being able to be used in UV LED devices. The emission spectra under 393 nm excitation, that corresponds to the 7F<sub>0</sub> → 5L<sub>6</sub> Eu<sup>3+</sup> transition, exhibit the set of 5D<sub>0</sub> → 7F<sub>0,1,2,3,4</sub> transitions in the red region attributed to the Eu<sup>3+</sup> in low-symmetry sites.<sup>47</sup> The sample doped with 4% has the highest relative emission, indicating that above this nominal doping percentage the quenching by concentration takes place. With the increase in Eu<sup>3+</sup> concentration, the distance between these ions decreases within the crystalline lattice, leading to an increase in the probability of energy transfer between the emitting centers. Thus, increasing the chances of a defect in the network being close to an europium center resulting in the deactivation through a non-radiative process.

The presence of the 5D<sub>0</sub> → 7F<sub>0</sub> transition in the emission spectra for all Eu<sup>3+</sup> percentages indicates that this ion is inserted in at least one site without inversion center since this transition, according to the symmetry selection rules is forbidden when Eu<sup>3+</sup> is occupying sites with inversion center. In order to elucidate the Eu<sup>3+</sup> ion occupation in the Ba<sub>2</sub>SiO<sub>4</sub> host, we measured some excitation spectra at 77 K within the range of the 5D<sub>0</sub> → 7F<sub>0</sub>(0–0) transition by fixing the emission wavelengths related to the different 5D<sub>0</sub> → 7F<sub>2</sub> components, these

Table 3 Bandgap values calculated from Kubelka–Munk approximation considering direct transitions for all synthesized samples

Sample	Bandgap/eV
Ba <sub>2</sub> SiO <sub>4</sub> :Eu <sup>3+</sup> (5%)	4.62
Ba <sub>2</sub> SiO <sub>4</sub> :Eu <sup>3+</sup> (4%)	4.80
Ba <sub>2</sub> SiO <sub>4</sub> :Eu <sup>3+</sup> (3%)	4.42
Ba <sub>2</sub> SiO <sub>4</sub> :Eu <sup>3+</sup> (2%)	4.38
Ba <sub>2</sub> SiO <sub>4</sub> :Eu <sup>3+</sup> (1%)	4.75
Undoped	5.82

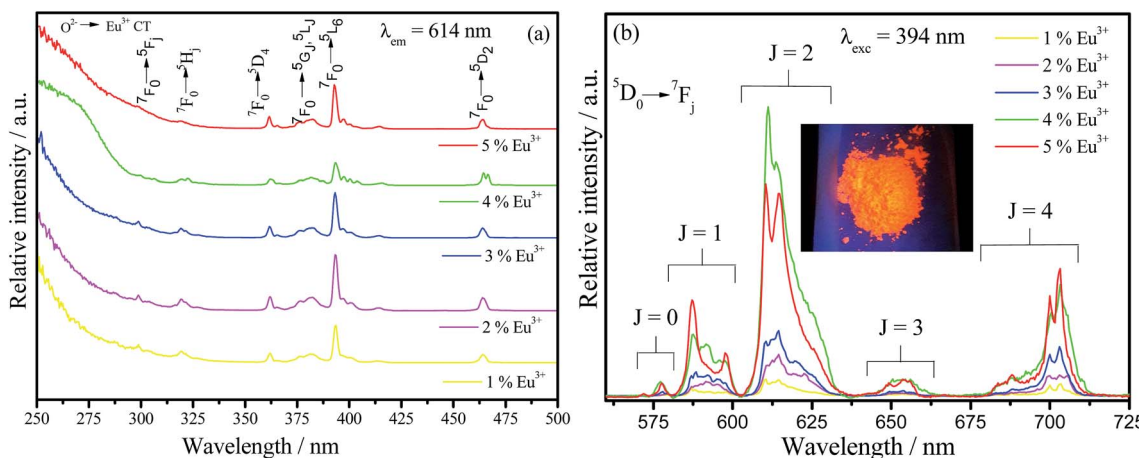


Fig. 6 Excitation (a) and emission (b) spectra of  $\text{Ba}_2\text{SiO}_4:\text{Eu}^{3+}$  powder samples measured at room temperature. Inset (b) is a photograph of the 4% doped sample under 270 nm UV light. The emission spectra at 250 nm are shown in Fig. ES6, in the ESI.†

spectra are shown in Fig. ES7.† For all samples, independently on the  $\text{Eu}^{3+}$  percentage, it is verified at least two maximum in the investigated range associated to 0–0 transition components. Thus, the presence of more than one 0–0 component confirms that  $\text{Eu}^{3+}$  is inserted in at least two non-equivalent sites without inversion center.

On the other hand, a detailed inspection in Fig. 6(b) reveals that just the 5% doped sample emission spectrum shows an anomalous profile. The region between 570 and 579 nm displays three components that can be associated to 0–0 transitions, one at 572 nm and the others at 577 and 579 nm. This profile is very similar to the one reported by A. M. Pires *et al.* (1997)<sup>20</sup> for  $\text{Eu}^{3+}$ -doped  $\text{Ba}_2\text{SiO}_4$  obtained from solid state route. In that case, emission spectrum exhibited two groups of transitions that have been related to the  ${}^5\text{D}_0 \rightarrow {}^7\text{F}_0$ , each group were assigned to two different emission centers, one of them characteristic of  $\text{Eu}^{3+}$  occupying  $\text{Ba}^{2+}$  sites and therefore, coordinated to the oxy ions belonging to the matrix structure, and the other one to the so called  $\text{Eu}^{3+}\text{O}^{2-}$  associates located in the interstices originated from a charge compensating mechanism due to the different oxidation states of  $\text{Ba}^{2+}$  and  $\text{Eu}^{3+}$ . However, in our case, it is not expected a charge compensation by oxi ions since we are using a charge compensation mechanism during the doping calculation. In order to evaluate this anomalous behavior, selective excitation spectra, Fig. 7(a), were performed at 77 K for the sample doped with 5% of  $\text{Eu}^{3+}$  fixing the emission in the different 0–0 components. When the emission wavelength is fixed in the anomalous 0–0 position (572 nm), Fig. 7(a), a charge transfer band (CT band) is observed at considerably lower energy (337 nm) when compared to the values for the  $\text{Eu}^{3+}$  in others lattices.<sup>48</sup> However, this CT band position (337 nm) is coincident with the one reported by A. M. Pires *et al.*<sup>20</sup> that was assigned to  $\text{Eu}^{3+}\text{O}^{2-}$  associates. In addition, the emission spectrum under 337 nm excitation, Fig. 7(b) exhibits an anomalous transition at 572 nm with the highest intensity in the spectrum that is attributed to a 0–0 transition originated in an europium ion located in a lattice interstice and associated with an oxy ion not bounded to

silicon.<sup>20</sup> On the other hand, when the emission is fixed at 579 nm, which is related to the  $\text{Eu}^{3+}$  occupying  $\text{Ba}^{2+}$  sites in the network, the CT band is located in the expected higher energy position, with maximum at 288 nm. Recently, K. Fiaczyk *et al.* discussed some peculiarities of  $\text{Eu}^{3+}$  luminescence in  $\text{Sr}_2\text{GeO}_4$ .<sup>49</sup> In this work authors claim that the presence of this  $\text{Eu}^{3+}\text{O}^{2-}$  associates are formed not only by the charge compensation mechanism, but also when host materials are rather loosely packed and/or contain chains constituted by the M–O polyhedral, and unfilled spaces that can locate oxy ions in its interstices. Therefore, in our case, it is feasible to correlate the arising of the  $\text{Eu}^{3+}\text{O}^{2-}$  associates to this explanation since that the  $\text{Ba}_2\text{SiO}_4$  matrix is indeed loosely packed containing Ba–O polyhedral chains with unfilled spaces, as previously reported in literature.<sup>26</sup> Furthermore, the dynamic air atmosphere applied during the calcination step increase the  $\text{O}_2$  concentration in the reactive environment, favoring the inclusion of extra oxi ions into the  $\text{Ba}_2\text{SiO}_4$  lattice.

To evaluate the anomalous intensity of 0–0 transition observed in Fig. 7(b), it is necessary to use an extension of Judd–Ofelt theory proposed by B. G. Wybourne<sup>50</sup> and M. C. Downer<sup>51</sup> and also approached by K. Fiaczyk *et al.* for evaluate  $\text{Eu}^{3+}\text{O}^{2-}$  associates in  $\text{Sr}_2\text{GeO}_4$ .<sup>49</sup> For this, it is necessary to consider that since the oxi ions not belonging to  $\text{SiO}_4$  tetrahedra may be located randomly in the host lattice, only a small fraction of  $\text{Eu}^{3+}$  ions encounters these oxi ions in their first coordination sphere, and only  $\text{Eu}^{3+}\text{O}^{2-}$  associates would show the low-energy CT transitions. This explains why this anomalous emission is only observed for the sample with the highest europium concentration. From this extended Judd–Ofelt theory, some specific symmetries can cause an increase of the 0–0 transition due to a slight contribution of the crystalline field Hamiltonian that occurs just when the charge transfer level has low energy. It appears that even a small linear contribution to the Hamiltonian crystal field may enhance the 0–0 transition probability if only the energy of CT state is low enough.<sup>49,52</sup> This effect occurs by a third order electric dipolar mechanism, which increase the intensity of 0–0 transition in relation to the other 0–

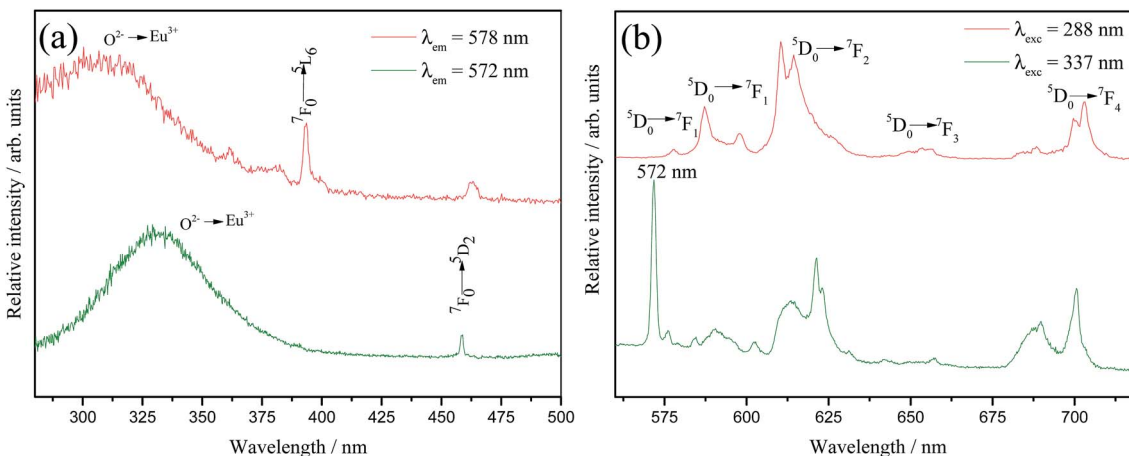


Fig. 7 Selective excitation (a) and emission (b) spectra of the sample  $\text{Ba}_2\text{SiO}_4:\text{Eu}^{3+}(5\%)$  measured at 77 K.

ones. However, the CT transition energy is just lowered when the  $\text{Eu}^{3+}$  ions are bounded to easily polarizable oxy ions and their electrons are not involved into other bonds. In our system these oxy ions with high polarizable environment are those not belonging to the  $\text{Ba}_2\text{SiO}_4$  lattice, and therefore introduced into the lattice interstices during the phase formation. Thus, these oxy ions with high polarizable environment decrease the CT energy and as consequence, when the excitation occurs at this CT specific position, the third order electric dipolar mechanism takes place, increasing the 0–0 intensity in relation to the other 0– $J$  transitions.<sup>49</sup> However, the  $\text{Eu}^{3+}\text{O}^{2-}$  associate concentration in the  $\text{Ba}_2\text{SiO}_4$  matrix is lower than that of  $\text{Eu}^{3+}$  sites replacing  $\text{Ba}^{2+}$ , causing little influence in the  $\text{Ba}_2\text{SiO}_4$  vibrational structure.

The intensity parameters  $\mathcal{Q}_2$  and  $\mathcal{Q}_4$  were also evaluated for all  $\text{Eu}^{3+}$  doped samples from the emission spectra measured at room temperature considering the method described by C. A. Kodaira *et al.*<sup>53</sup> and they are summarized in Table 4. The 0–2 and 0–4 transitions are related to  $\mathcal{Q}_2$  and  $\mathcal{Q}_4$ , respectively, and the 0–1 transition is taken as reference, for this transition being allowed by magnetic dipole and its intensity does not vary with external electric field changes caused by the crystal/ligand field. Considering the integrated areas below the transitions  ${}^5\text{D}_0 \rightarrow {}^7\text{F}_J$  with  $J = 2, J = 4$ , and  $J = 1$  it is possible to write:

$$A_{0-\lambda} = A_{0-J} = A_{01} \frac{I_{0-J}}{I_{0-1}} \frac{h\nu_{0-1}}{h\nu_{0-J}} \quad (4)$$

$$\sum_{\lambda=2,4} \mathcal{Q}_\lambda \left\langle {}^5\text{D}_0 \parallel \text{U}^{(\lambda)} \parallel {}^7\text{F}_J \right\rangle^2 = A_{01} \frac{I_{0-J}}{I_{0-1}} \frac{h\nu_{0-1}}{h\nu_{0-J}} \frac{3hc^3 4\epsilon_0}{64\pi^3 e^2} \frac{1}{v_\lambda^3 x} \quad (5)$$

where the square reduced matrix elements  $\langle {}^5\text{D}_0 \parallel \text{U}(\lambda) \parallel {}^7\text{F}_J \rangle^2$  are 0.0032 for  $\mathcal{Q}_2$  and 0.0023 for  $\mathcal{Q}_4$ ;<sup>53</sup>  $e$  is the electron charge,  $h$  and  $\epsilon_0$  are the Planck's and vacuum permittivity constants, respectively;  $c$  is the speed of light in vacuum;  $A_{01}$  is the Einstein's coefficient for spontaneous emission which value can be estimated considering the expression  $A_{01} = 14.65n^3$  in  $\text{s}^{-1}$  (ref. 54) taken into account the refractive index ( $n$ ) that in this case equals 1.7 and so the correspondent  $A_{01}$  value is  $71.97 \text{ s}^{-1}$ ; the term  $I_{0-J}$  is the area under the curve related to the  ${}^5\text{D}_0 \rightarrow {}^7\text{F}_J$  transitions

obtained from the spectral data and  $x$  is the Lorentz local field correction, given by the expression  $n(n^2+2)^2/9$ .<sup>55</sup> The  $\mathcal{Q}_2$  parameter may be associated with  $\text{Eu}^{3+}$  site distortions because the electric dipole  ${}^5\text{D}_0 \rightarrow {}^7\text{F}_2$  transition relative intensity is dependent on the  $\text{Eu}^{3+}$  local symmetry.<sup>56</sup> Also,  $\mathcal{Q}_4$  values are straightly related to the Eu–O angular deformations.<sup>57</sup> In this way, the relative intensity of this hypersensitive transition increases with the decrease of  $\text{Eu}^{3+}$  local symmetry and site distortion.<sup>53</sup> On the other hand, the  $\mathcal{Q}_4$  parameter is influenced by the electron density of the ligands ( $L$ ) around  $\text{Eu}^{3+}$ .<sup>58</sup> The  $\mathcal{Q}_4$  parameter is less sensitive to small angular changes, but it is more sensitive to the separation between the metal ion and the ligand donor.<sup>57</sup> So, the relatively low values of  $\mathcal{Q}_2$  intensity parameters for all samples showed in Table 4 indicate that the chemical environment around  $\text{Eu}^{3+}$  is relatively symmetric, since the values are lower compared to other systems that  $\text{Eu}^{3+}$  ions are in low symmetry sites.<sup>59</sup> These relative low values are expected when we compare the emission intensity of the 0–1 and 0–2 transitions.

In order to understand the intensity parameters behavior, it is necessary to evaluate the symmetry around  $\text{Eu}^{3+}$  ions with CN 9 and 10. In the literature it is shown that different kinds of barium-containing silicates usually have symmetric sites, especially those with CN 10,<sup>60</sup> justifying the low  $\mathcal{Q}_2$  values for the system. Also, L. Lin *et al.*<sup>61</sup> performed a detailed structural study for the same material doped with another lanthanide, the  $\text{Ce}^{3+}$  doped- $\text{Ba}_2\text{SiO}_4$  phosphor, in which the  $\text{Ce}^{3+}$  substitution causes a decrease in the average bond length of 0.994% and a bond angle average deviation of  $\pm 0.185^\circ$ . In this context, we can assume that the site deformation around  $\text{Eu}^{3+}$  ions is very low, justifying the low  $\mathcal{Q}_2$  values and suggesting that the main contribution to the structural defects observed by FTIR, Raman and DRS comes from the barium vacancy defects. Samples doped with 1, 2, 3 and 4% have similar values of  $\mathcal{Q}_2$ , however, the  $\mathcal{Q}_2$  value for the 5% doped sample is quite lower due to the presence of the  $\text{Eu}^{3+}\text{O}^{2-}$  associate. The transition mechanism for these associates is different, as mentioned before, favoring the 0–0 transition in detriment of the all other 0– $J$  transitions. The decrease in the 0–2 band intensity results in a decrease of the calculated  $\mathcal{Q}_2$  value.



**Table 4** Experimental Judd–Ofelt intensity parameters ( $\Omega_2$ ,  $\Omega_4$ ), and lifetime values considering a bi-exponential decay ( $\tau_1$  and  $\tau_2$ ); the pre-exponential factor for each lifetime value ( $A_1$  and  $A_2$ ); radiative ( $A_{\text{rad}}$ ) and total ( $A_{\text{rad}} + A_{\text{nrad}}$ ) decay rate and quantum efficiency ( $\eta$ ) for the prepared phosphors

$\text{Ba}_2\text{SiO}_4$	$\Omega_2^a$ (pm $^2$ )	$\Omega_4^a$ (pm $^2$ )	$\tau_1^b$ (ms)	$A_1$	$\tau_2^b$ (ms)	$A_2$	$R^{2c}$	$\langle \tau \rangle$ (ms)	$A_{\text{total}}$ (s) $^{-1}$	$A_{\text{rad}}^d$ (s) $^{-1}$	$\eta^e$ (%)
5% Eu $^{3+}$	5.1	4.3	0.12	$7.9 \times 10^5$	1.76	$9.2 \times 10^5$	0.99	1.66	602	437	72.6
4% Eu $^{3+}$	6.2	6.1	0.14	$2.5 \times 10^5$	1.59	$1.0 \times 10^5$	0.99	1.34	746	509	68.2
3% Eu $^{3+}$	6.2	7.2	0.25	$5.4 \times 10^5$	1.51	$6.9 \times 10^5$	0.99	1.29	901	530	58.8
2% Eu $^{3+}$	6.4	5.6	0.17	$4.0 \times 10^6$	1.34	$2.1 \times 10^6$	0.99	1.11	901	501	55.6
1% Eu $^{3+}$	5.9	5.9	0.19	$3.2 \times 10^6$	1.57	$1.8 \times 10^6$	0.99	1.33	752	500	66.5

<sup>a</sup> Values calculated from emission spectra under  $\lambda_{\text{exc}} = 250$  nm. <sup>b</sup> Lifetime values calculated fixing excitation wavelength at 250 nm and emission wavelength at 614 nm ( ${}^5\text{D}_0 \rightarrow {}^7\text{F}_2$ ). <sup>c</sup> Goodness of fit coefficient for bi-exponential. <sup>d</sup> Radiative rate calculated from emission spectra under  $\lambda_{\text{exc}} = 250$ . <sup>e</sup> Quantum efficiency calculated from the average lifetime values, and the emission spectra under  $\lambda_{\text{exc}} = 250$  nm.

The low  $\Omega_4$  values for all samples compared to other systems<sup>58,59</sup> show the low polarizable environment around Eu $^{3+}$  ions, suggesting a low covalence degree for the Eu–O bond. The  $\Omega_4$  parameter is the lowest for the 5%-doped phosphor, due to the decrease of the 0–4 transition intensity caused by the presence of the Eu $^{3+}$ –O $^{2-}$  associate. The other differences in the  $\Omega_4$  values must be correlated to small differences in the Eu–O bond distance which directly influence the electron density around Eu $^{3+}$  ions.

Emission lifetime measurements were performed at room temperature for the Eu $^{3+}$ -doped Ba<sub>2</sub>SiO<sub>4</sub> samples, and the obtained curves, Fig. ES8,† were adjusted by using a multi-exponential fit that yielded two experimental lifetime values listed in Table 4. These lifetime values were used to estimate the quantum efficiency also included in Table 4. The quantum efficiency of an emitter state ( $\eta$ ) is defined as the ratio between the radiative ( $A_{\text{rad}}$ ) and the total contributions (radiative and non-radiative,  $A_{\text{nrad}}$ ), as represented in eqn (6).<sup>62</sup>

$$\eta = \frac{A_{\text{rad}}}{A_{\text{rad}} + A_{\text{nrad}}} \quad (6)$$

$A_{\text{rad}}$  values are determined by the sum of the main radiative contributions to the Eu $^{3+}$  transitions, eqn (7), and  $A_{\text{nrad}}$  values by using eqn (8), in which the average experimental lifetime  $\langle \tau \rangle$ , defined by eqn (9), is taking into account. In this last equation, the term  $A_i$  is the pre-exponential factor, or amplitude associate to each lifetime ( $\tau_i$ ) values.<sup>63</sup>

$$A_{\text{rad}} = \sum_J A_{0-J} \quad (7)$$

$$A_{\text{total}} = \frac{1}{\langle \tau \rangle} = A_{\text{rad}} + A_{\text{nrad}} \quad (8)$$

$$\langle \tau \rangle = \frac{\sum A_i \tau_i^2}{\sum A_i \tau_i} \quad (9)$$

The average lifetime  $\langle \tau \rangle$  values listed in Table 4 for all samples lies in the 1.01–1.80 ms range, which are in agreement with lifetime values related to the  ${}^5\text{D}_0$  excited state for Eu $^{3+}$ -doped Ba<sub>2</sub>SiO<sub>4</sub> reported by A. M. Pires *et al.*<sup>21</sup> The fact that all samples have at least two distinct lifetimes values confirms that the emission is starting from Eu $^{3+}$  occupying at least two different non-equivalent

sites. In addition, lifetime varies non-linearly with the variation of Eu $^{3+}$  concentration due to the generation of intermediate energy levels, such as the defects mentioned before, that mediates the energy transfer mechanisms affecting the  ${}^5\text{D}_0$  decay rates.<sup>64</sup>

The prepared Ba<sub>2</sub>SiO<sub>4</sub>:Eu $^{3+}$  phosphors, especially the one doped with 5%, show a relative high quantum yield of luminescence ( $\eta$ ) when compared to other host lattices such as CaSiO<sub>3</sub>:Eu $^{3+}$  ( $\eta \sim 33\%$ ),<sup>65</sup> Zn<sub>2</sub>SiO<sub>4</sub>:Eu $^{3+}$  ( $\eta \sim 30\%$ ),<sup>66</sup> and BaAl<sub>2</sub>O<sub>4</sub>:Eu $^{3+}$  ( $\eta \sim 70\%$ )<sup>67</sup> whereas Eu $^{3+}$  is also replacing cations oxidation state of +2. Furthermore, to the best of our knowledge, the Eu $^{3+}$  quantum efficiency in the Ba<sub>2</sub>SiO<sub>4</sub> matrix was not reported yet. Finally, it is important to highlight that the CIE (International Commission on Illumination) chromaticity diagrams<sup>68</sup> built for all the produced phosphors (see Fig. ES9†) guarantee high red color purity, in special related to the one doped with 4% which chromaticity coordinate values are  $x = 0.67$  and  $y = 0.32$ , with 100% of color purity at 394 nm.

## Conclusion remarks

In summary, Eu $^{3+}$ -doped Ba<sub>2</sub>SiO<sub>4</sub> single-phase powder red phosphor was successfully synthesized using softer condition through a novel approach based on an adapted sol–gel methodology than the standard solid-state route that requires higher temperatures and longer synthesis time. Besides that, a detailed spectroscopic study not reported yet was provided for this system by using Eu $^{3+}$  as spectroscopic probe in order to optimize structural and optical properties of the phosphor aiming light emitting diodes application. Under 250 nm excitation, the phosphors exhibit an intense red emission due to the Eu $^{3+}$  *f*–*f* transitions, and the 4%-doped sample shows the highest relative emission intensity and the 5%-doped the highest quantum efficiency (72.6%), what make of these two samples the most suitable for use in WLED application under UV excitation.

## Conflicts of interest

There are no conflicts to declare.

## Acknowledgements

The authors are thankful to the Brazilian agencies FAPESP, CNPq and CAPES for the financial research support. Airton G. B.



Junior is particularly grateful to the São Paulo research Foundation (FAPESP) for the award of some scholarships (Grant No. 2012/13876-9, 2015/10394-1, and 2016/20421-9). Laboratório de Microscopia Eletrônica de Varredura (FCT-UNESP), research group in sol-gel (UNIFRAN), Laboratório de Filmes Nanoestruturados e Espectroscopia (FCT-UNESP), and Laboratório de compósitos e cerâmicas funcionais (FCT-UNESP).

## References

- J. H. Oh, S. J. Yang, Y. Sung and Y. R. Do, *Opt. Express*, 2012, **20**, 20276.
- H. Ji, L. Wang, M. S. Molokeev, N. Hirosaki, R. Xie, Z. Huang, Z. Xia, O. M. ten Kate, Li. Liub and V. V. Atuchin, *J. Mater. Chem. C*, 2016, **4**, 6855.
- N. Guo, C. Jia, J. Li, Y. Zhao, R. Ouyang and W. Lu, *RSC Adv.*, 2015, **5**, 46517.
- J. Liu, H. Lian, H. J. Sun and C. Shi, *Chem. Lett.*, 2005, **34**, 1340.
- H. Pan, X. Li, J. Zhang, L. Guan, H. Su and F. Teng, *Mater. Lett.*, 2015, **155**, 106.
- C. Sun, Y. Chang, Y. Wang, C. Chen, Y. Lo and H. Cheng, *J. Disp. Technol.*, 2015, **11**, 261.
- E. F. Schubert and J. K. Kim, *Science*, 2005, **208**, 1274.
- N. A. Fromer and M. S. Diallo, *J. Nanopart. Res.*, 2013, **15**, 2044.
- F. Xie, Z. Dong, D. Wen, J. Yan, J. Shi, J. Shi and M. Wu, *Ceram. Int.*, 2015, **41**, 9610.
- Y. K. Su, S. J. Chang, S. C. Wei and S. Chen, *IEEE Trans. Device Mater. Reliab.*, 2005, **5**, 277.
- L. Chen, C. Lin, C. Yeh and R. Liu, *Materials*, 2010, **3**, 2172.
- X. Bai, G. Caputo, Z. Hao, V. T. Freitas, J. Zhang, R. L. Longo, O. L. Malta, R. A. S. Ferreira and N. Pinna, *Nat. Commun.*, 2014, **5**, 5702.
- S. Ye, F. Xiao, Y. X. Pan, Y. Y. Ma and Q. Y. Zhang, *Mater. Sci. Eng., R*, 2010, **71**, 1.
- S. H. M. Poort, H. M. Reijnhoudt, H. G. T. Van Der Kuip and G. Blasse, *J. Alloys Compd.*, 1996, **241**, 175.
- L. C. Ferracin, M. R. Davolos and L. A. O. Nunes, *J. Lumin.*, 1997, **72**, 185.
- Y. Tang, S. Hu, C. C. Lin, N. C. Bagkar and R. Liu, *Appl. Phys. Lett.*, 2007, **90**, 151108.
- P. Haro-González, M. Karlsson, S. M. Gaita, C. S. Knee and M. Bettinelli, *Solid State Ionics*, 2013, **247**, 94.
- C. E. Secu, R. F. Negrea and M. Secu, *Opt. Mater.*, 2013, **35**, 2456–2460.
- G. Gasparotto, M. A. Cebim, M. S. Goes, S. A. M. Lima, M. R. Davolos, J. A. Varela, C. O. Paiva-Santos and M. A. Zaghete, *J. Appl. Phys.*, 2009, **106**, 063509.
- A. M. Pires, M. R. Davolos and O. M. L. Malta, *J. Lumin.*, 1997, **72**, 244.
- A. M. Pires and M. R. Davolos, *Chem. Mater.*, 2001, **13**, 21.
- Z. Wang, S. Guo, Q. Li, X. Zhang, T. Li, P. Li, Z. Yang and Q. Guo, *Phys. B*, 2013, **411**, 110.
- B. Ritter, T. Krahl, K. Rurack and E. Kemnitz, *J. Mater. Chem. C*, 2014, **2**, 8607–8613.
- F. Gao, Y. Sheng, Y. Song, K. Zheng, C. Lin, H. Zhang, Q. Huo and H. Zou, *J. Sol-Gel Sci. Technol.*, 2014, **71**, 313.
- J. E. Ghoul, K. Omri, S. A. Gómez-Lopera and L. E. Mir, *Opt. Mater.*, 2014, **36**, 1034–1039.
- J. K. Han, M. E. Hannah, A. Piquette, J. B. Talbot, K. C. Mishra and J. McKittrick, *J. Lumin.*, 2013, **133**, 184.
- J. K. Han, M. E. Hannah, A. Piquette, J. B. Talbot, K. C. Mishra and J. McKittrick, *ECS J. Solid State Sci. Technol.*, 2012, **1**, 98.
- A. Birkel, N. A. DeCino, N. C. George, K. A. Hazelton, B. Hong and R. Seshadri, *Solid State Sci.*, 2013, **19**, 51.
- P. A. Raymundo-Pereira, D. A. Ceccato, D. A. G. B. Junior, M. F. S. Teixeira, S. A. M. Lima and A. M. Pires, *RSC Adv.*, 2016, **6**, 104529.
- M. Zhang, J. Wang, Q. Zhang, W. Ding and Q. Su, *Mater. Res. Bull.*, 2007, **42**, 33.
- G. Xia, S. Zhou, J. Zhang, S. Wang, Y. Liu and J. Xu, *J. Cryst. Growth*, 2005, **283**, 257.
- C. H. Park, S. J. Park, B. Y. Yu, H. S. Bae, C. H. Kim, C. H. Pyun and H. G. Yan, *J. Mater. Sci. Lett.*, 2000, **19**, 335.
- K. A. Denault, J. Brzoch, S. D. Kloß, M. W. Gaultois, J. Siewenie, K. Page and R. Seshadri, *ACS Appl. Mater. Interfaces*, 2015, **7**, 7264.
- J. S. Kim, P. E. Jeon, J. C. Choi and H. L. Park, *Solid State Commun.*, 2005, **133**, 187.
- S. Yao, L. Xue and Y. Yan, *Ceram.-Silik.*, 2011, **55**, 251.
- S. Chen, S. L. Liu, M. Gu, C. Ni, B. Liu and S. Huang, *J. Lumin.*, 2013, **140**, 1.
- D. Theyvaraju, S. Muthukumaran and M. Ashokkumar, *J. Mater. Sci.: Mater. Electron.*, 2013, **24**, 5189.
- H. F. N. Oliveira, R. B. Trinca and Y. Gushikem, *Quim. Nova*, 2009, **32**, 1346.
- M. Handke and M. Urban, *J. Mol. Struct.*, 1982, **79**, 353.
- A. C. S. Silva, G. G. Souza, M. A. L. Nobre and A. M. Pires, *J. Mater. Sci.*, 2010, **45**, 4216.
- M. V. Abrashev, N. D. Todorow and J. Geshew, *J. Appl. Phys.*, 2014, **116**, 103508.
- M. Zhang, J. Wang, Q. Zhang, W. Ding and Q. Su, *Mater. Res. Bull.*, 2007, **42**, 33.
- C. Barthou, J. Benoit, P. Benalloul and A. A. Morell, *J. Electrochem. Soc.*, 1994, **141**, 524.
- A. B. Murphy, *Sol. Energy Mater. Sol. Cells*, 2007, **91**, 1326.
- P. Kubelka and F. Munk, *Z. Tech. Phys.*, 1931, **15**, 593.
- S. Z. Karazhanov, P. Ravindran, P. Vajeeston, A. Ulyashin, H. Fjellvag and B. G. Svensson, *J. Appl. Phys.*, 2009, **106**, 123701.
- W. T. Carnall, G. L. Goodman, K. Rajnak and R. S. Rana, *J. Chem. Phys.*, 1989, **90**, 3443.
- D. Van Der Voort, G. J. Dirksen and G. Blasé, *J. Phys. Chem. Solids*, 1992, **53**, 219.
- K. Fiaczyk and E. Zych, *RSC Adv.*, 2016, **6**, 91836.
- B. G. Wybourne, *J. Chem. Phys.*, 1968, **48**, 2596.
- M. C. Downer, G. W. Burdick and D. K. Sardar, *J. Chem. Phys.*, 1988, **89**, 1787–1797.
- X. Y. Chen and G. K. Liu, *J. Solid State Chem.*, 2005, **178**, 419–428.



53 C. A. Kodaira, H. F. Brito, O. L. Malta and O. A. Serra, *J. Lumin.*, 2003, **101**, 11.

54 A. P. Duarte, M. Gressier, M. Menu, J. Dexpert-Ghys, J. M. A. Caiut and S. J. L. Ribeiro, *J. Phys. Chem. C*, 2012, **116**, 505.

55 A. M. Pires, M. R. Davolos and E. B. Stucchi, *Int. J. Inorg. Mater.*, 2001, **3**, 785.

56 W. T. Carnall, *Handbook on the physics and chemistry of rare earths*, 1979, vol. 3, p. 171.

57 R. T. Moura, A. N. C. Neto, R. L. Longo and O. L. Malta, *J. Lumin.*, 2016, **170**, 420.

58 T. Grzyb and S. Lis, *Inorg. Chem.*, 2011, **50**, 8112.

59 A. M. Pires, M. R. Davolos and E. B. Stucchi, *Int. J. Inorg. Mater.*, 2001, **3**, 785.

60 N. C. George, K. A. Denault and R. Seshadri, *Annu. Rev. Mater. Res.*, 2014, **43**, 481.

61 L. Lin, L. X. Huang, R. Shi, W. Zhou, Y. Huang, J. Zhong, Y. Tao, J. Chen, L. Ning and H. Liang, *RSC Adv.*, 2017, **7**, 25685.

62 O. L. Malta, S. J. L. Ribeiro, M. Faucher and P. Porcher, *J. Phys. Chem. Solids*, 1991, **52**, 587.

63 Y. Ma, H. Wang, W. Liu, Q. Wan, J. E. Xu and Y. Tang, *J. Phys. Chem. B*, 2009, **113**, 14139.

64 R. A. S. Ferreira, M. Nolasco, A. C. Roma, R. L. Longo, O. L. Malta and L. D. Carlos, *Chem.-Eur. J.*, 2012, **18**, 12130.

65 L. Zhou and B. Yan, *J. Phys. Chem. Solids*, 2008, **69**, 2877.

66 L. Dacanin, S. R. Lukic, D. M. Petrovic, M. Nikolic and M. D. Dramicanin, *Phys. B*, 2011, **406**, 2319–2322.

67 R. J. Wiglusz and T. Grzyb, *Opt. Mater.*, 2013, **36**, 539–545.

68 P. A. Santa-cruz and F. S. Teles, *Spectra Lux Software. Versão 1.0 RENAMI*, U. Federal de Pernambuco, 2003.

